PFC/JA-89-1

Observations of Field Profile Modifications in a Raman Free Electron Laser Amplifier

K.Xu, G.Bekefi, and C.Leibovitch

January 1989

Department of Physics, Plasma Fusion Center
and
Research Laboratory of Electronics

Massachusetts Institute of Technology
Cambridge, Massachusetts 02139 USA

This work was supported by the Air Force Office of Scientific Research and the National Science Foundation.

Submitted for publication in: The Physics of Fluids.

OBSERVATIONS OF FIELD PROFILE MODIFICATIONS IN A RAMAN FREE ELECTRON LASER AMPLIFIER

K. Xu†, G. Bekefi, and C. Leibovitch‡

Department of Physics and Research Laboratory of Electronics
Massachusetts Institute of Technology
Cambridge, Massachusetts 02139

ABSTRACT

We report measurements of the spatial distribution of the RF electric field intensities and phases induced in a free electron laser (FEL) amplifier operating in the collective (Raman) regime. The studies are carried out at a microwave frequency of ~10 GHz in a FEL using a mildly relativistic electron beam of ~200 keV energy and 1 - 4 A current. The probing of the ponderomotive (space charge) and the electromagnetic waves is accomplished by means of small movable electric dipole antennas inserted into the interaction region.

† permanent address: University of Electronic Science and Technology of China, Chengdu, China.

‡ permanent address: Applied Physics Department, Scientific Division, Rafael Laboratory, Haifa 31021, Israel.

1. INTRODUCTION

Free electron laser (FEL) amplification is the consequence of a resonant interaction [1] between an incident electromagnetic wave and a co-propagating electron beam that has been injected into a periodic "wiggler" magnetic field. This can lead to high output gain, and high efficiency of converting electron beam kinetic energy into radiation. Remarkably, it also leads to large phase shifts [2]-[4] in the amplified electromagnetic wave. Under proper circumstances this phase shift can have a sign such that the electromagnetic wave is refracted towards the axis of the electron beam in a manner somewhat akin to the guiding properties of an optical fiber. Such "optical guiding" [5]-[10] would mitigate the effects of diffraction, and thereby allow the length of FEL wigglers to exceed the Rayleigh range. Long wigglers are needed if free-electron lasers are to operate either in the vacuum-ultraviolet or at high efficiencies in the infrared wavelength regime.

It comes as no surprise that strong FEL activity as described above should be accompanied by significant modification of the spatial distribution of the RF fields within and in the immediate vicinity of the electron beam. To be sure, one way of confirming optical guiding is by observation of the changes in the transverse spatial profile of the copropagating amplified wave. Such field probing can be quite difficult at short wavelengths (infrared and visible). However, the microwave regime, in which our experiments are conducted, offers a relatively simple and direct way. We allow small, movable electric dipole antennas to traverse the waveguide in which the interaction takes place. Using antennas sensitive to different polarizations, we are then able to distinguish between wave types.

There are two major wave types in the vicinity of the bunched electron beam to which our electric dipoles respond. First, there are the electromagnetic (solenoidal) fields associated with the growing electromagnetic wave of frequency ω and axial wavenumber $k_{||}$, propagating with a velocity $v_p = (\omega/k_{||}) \geq c$. And then there are the irrotational, quasi-electrostatic fields of the bunched electron beam propagating with a phase velocity $\omega/(k_{||} + k_w)$ approximately equal to the electron beam velocity $v_b < c$ ($k_w = 2\pi/l_w$ is the wiggler wave number). In the case of tenuous, highly relativistic beams used in short wavelength FELs, the contribution of the space charge electric field to the overall field

profile is usually very small. However, in the microwave regime where often high current, mildly relativistic beams are employed, the contribution from the space charge electric field may no longer be negligible, as will be demonstrated in the experiments described below.

In section 2 of this paper we describe the experimental arrangement. In section 3 we present field profile measurements (in amplitude and phase) associated with the space charge wave. In section 4 we give profiles associated primarily (but not entirely) with the electromagnetic wave. The observations will be discussed in section 5.

2. EXPERIMENTAL SET UP

Figure 1 shows a schematic of our experiment. The accelerating potential is supplied by a Marx generator (Physics International Pulserad 615MR) which has a maximum capability of 500kV and 4kA. Since this accelerator does not use a pulse-forming network, the output voltage pulse is essentially that of a discharging capacitor bank with a shunt adjusted RC time constant of $10-100\mu$sec. The electron beam is generated by a thermionically emitting, electrostatically focused, Pierce-type electron gun (250 kV, 250 A) from a SLAC klystron (model 343). An assembly of focusing coils transports the electron beam into the drift tube. To insure good electron orbits, an aperture acting as an emittance selector is inserted which limits the electron beam radius to $r_b = 0.245$ cm so that only the inner portion of the beam is used. With this precaution, the energy spread of the beam entering the magnetic wiggler is $\Delta\gamma_{||}/\gamma_{||} \leq 0.003$ ($\gamma_{||} = [1 - v_{||}^2/c^2]^{-\frac{1}{2}}$).

The gun focusing coils guide the electron beam into a rectangular (1.01 cm $\times$2.29 cm) stainless steel evacuated drift tube which is also the waveguide for the electromagnetic radiation. The beam is contained by an uniform axial magnetic field $B_{||}$ that has a power supply limited maximum of 7 kG and a minimum of approximately 800 G. Below this value, beam defocusing and deterioration occur. The net beam current entering the magnetic wiggler is in the range of 1-5 A. The 65 period wiggler magnet has a period $l_w = 3.5$ cm, a maximum amplitude $B_w = 1.0$ kG, and is generated by bifilar conductors. Since the beam aperture limits the size of the beam to $r_b/l_w \approx 0.07$, the wiggler field is close to that of an ideal wiggler. That is, the effects of the radial variation of the wiggler field

and the presence of the off-axis components are usually small. At the wiggler entrance a slowly increasing field amplitude is produced by resistively loading the first six periods of the wiggler magnet [11].

The 2.7 m long drift tube acts as a rectangular waveguide whose fundamental TE_{10} mode has a cutoff frequency of $\omega_c/2\pi = 6.6$ GHz. Microwaves are launched onto the electron beam by a waveguide coupler (see Fig. 1). All our measurements are carried out at frequencies between 9 and 11 GHz. At these frequencies the empty waveguide can support only the fundamental (TE_{10}) mode, all higher modes being evanescent. The monochromatic radiation injected into the system is provided by a low power variable frequency source and amplified by means of a traveling wave tube amplifier. Typical power inputs into the FEL are in the 1 - 10 W range. At the output end of the wiggler, a mica window transmits the linearly polarized radiation generated in the drift tube, where it is measured by means of standard calibrated crystal detectors.

The transverse profile of the RF fields is studied by means of three small electric dipole antennas inserted into the waveguide as is illustrated in Figs. 1(b), (c). Two of the antennas, inserted through stainless steel bellows, are movable along the x axis, and their positions are precision controlled by micrometer screws. The third, reference antenna is fixed and protrudes slightly into the waveguide wall as is seen in Figs. 1(b), (c). Each probe has a length of 0.1 cm; cold tests show that the probes can detect RF intensity variations as small as 1% over distances of $\simeq$ 0.05 cm. The signal from each probe is attenuated by a variable attenuator, then measured by a calibrated crystal detector. The outputs from the crystal rectifiers are then displayed on fast oscilloscopes. We note that all three antennas are roughly in the middle of the wiggler region and in exactly the same transverse plane, $z \approx 115$ cm from the upstream end of the wiggler.

The left hand movable antenna designated in Figs. 1(b), (c) by I_y(EM) probes the y component of the RF electric field intensity, as does the reference probe I_y(REF). Cold test carried out in the absence of the FEL interaction show that the I_y(EM) probe accurately maps out the TE_{10} waveguide mode whose electric field amplitude is shown schematically in Fig. 1(b), and is given by the familiar expression, $E_y(x,t) = E_{0y}cos(\pi x/a)cos(\omega t - k_{\|}z)$, $-a/2 \leq x \leq a/2$ where $a = 2.29$ cm equals the length of the wide dimension of the

waveguide. Therefore the probe designated I_y(EM) maps out primarily the RF profile associated with the electromagnetic wave launched into the interaction region. The fixed reference probe I_y(REF) likewise measures primarily the electromagnetic field intensity of the launched, amplified wave.

The right hand movable antenna, designated I_x(SC), is sensitive to the x component of any RF electric field. Cold tests indicate that because of slight misalignment, a small signal due to E_y is nonetheless present on this probe. However, this intensity is more than 25 dB below the intensity of the y component and thus causes no problems in the measurements described below.

During FEL activity, the presence of x-directed electric fields is due mainly to the quasi-electrostatic, irrotational fields of the bunched electrons, whose spatial distribution is illustrated schematically in Fig. 1(c). Higher order waveguide modes with electric field components in the x direction could also be present during FEL activity, but calculations show [12] that their expected amplitudes are very small compared with the space charge fields.

In addition to intensity profiles, we have also measured the profiles of the RF phase. This is accomplished by standard interferometric techniques [2]-[4] in which the antenna signal is mixed in a "magic tee" with a reference signal from the TWT launcher.

Typical oscilloscope traces of the intensity and phase are illustrated in Fig. 2. The FEL is fired by the discharging of the Marx accelerator. Because of an RC droop, the beam energy falls gradually as is illustrated in Fig. 2(a). Amplification [Fig. 2(b)], as measured by the y-oriented reference probe I_y(REF) occurs at a beam energy for which the slow (negative energy) space-charge wave on the beam is near phase synchronism with the electromagnetic wave. This results in the gain peak. The gain is $\sim$3 dB. Later in time, at a lower beam energy, one observes a dip corresponding to wave absorption. Here the wave energy is converted to electron kinetic energy, as is known to occur when the fast (positive energy) space-charge wave is in synchronism with the electromagnetic wave.

The resonance relationship between the guided electromagnetic wave and the wave on the beam is given by the well known expressions

$$\omega^2 = c^2 k_{\|}^2 + \omega_c^2 \tag{1}$$

and

$$\omega = (k_{||} + k_w)\beta_{||}c \pm p_1\omega_p\phi^{1/2}/\gamma_{||}\gamma^{1/2}, \tag{2}$$

where the plus sign corresponds to the fast, positive energy, "passive" space charge wave, and the minus sign corresponds to the slow, negative energy, "active" space charge wave; $\omega_c^2 = \omega_{c0}^2 + p_2\omega_p^2/\gamma$ is the effective waveguide cutoff frequency adjusted for the presence of the electron beam; ω_{c0} is the empty waveguide cutoff frequency [(in our case the lowest mode of a rectangular waveguide (TE_{10})]; $k_w = 2\pi/l_w$ is the wiggler wavenumber; $\beta_{||} = v_{||}/c$ is the normalized axial velocity of the electron beam, and $\omega_p = (Ne^2/m_0\epsilon_0)^{1/2}$ is the nonrelativistic plasma frequency. The relativistic mass increase $\gamma = 1 + eV/m_0c^2$ measures the beam energy; ϕ is the adjustment [13] to the plasma frequency due to the combined wiggler and axial magnetic fields; p_1 is the reduction in the plasma frequency that results from finite radial effects, and p_2 is the electromagnetic wave energy weighted ratio of the electron beam cross-section and the waveguide area. In normal operation of our FEL, $p_2 \approx 0.06$ so that $\omega_c \approx \omega_{c0}$, $p_1 \approx 0.5$, and $\phi \approx 1$.

Fig. 2(c) shows the corresponding oscilloscope trace as observed with the space charge probe I_x(SC). As expected, it shows maximum activity at times when the electromagnetic wave interacts either with the slow or fast space charge waves.

Fig. 2(d) shows the temporal behavior of the RF phase of the electromagnetic wave. It is noteworthy that maximum phase change occurs at a time when the gain is close to zero, as is characteristic of FELs operating in the collective (Raman) regime [2].

In order to check the validity of these results, we dump the electron beam into the waveguide walls by means of a magnetic kicker placed 18 cm upstream of the probes. This allows the FEL-induced profile modification of the RF field to convert down to the fundamental TE_{10} mode, and null signals result (the higher modes excited by the FEL interaction are evanescent and die out exponentially within 1 or 2 waveguide wavelengths from the kicker position).

The experiments described below are carried out on electron beams with energy ranging from 150-170 keV and a current of ~1 A. The axial guide magnetic field is held constant

at 1580 G. The wiggler field amplitude is set at one of two values, 130 G and 200 G. The RF input signal has a frequency of 9.7 GHz and a power level of 3 W. With these parameters, the FEL operates in the linear regime and has a single pass gain of $\sim$ 3 dB at the axial position $z \approx 115$ cm from the beginning of the wiggler, where the antennas are located.

3. SPACE-CHARGE FIELD PROFILES

The spatial distribution of the DC current density $J_z(x,y)$ of the electron beam is determined by using the space charge dipole antenna (designated I_x(SC) in Fig. 1) as a current monitor. This is accomplished by terminating the coaxial cable from the antenna with a 50 Ohm load and measuring the voltage across it. Figure 3(a) illustrates the current density profile $J_z(x,0)$ as a function of displacement of the antenna in the x direction. We see that the full width of the distribution at half maximum is $\sim$5 mm, and equals the diameter of the emittance selector placed upstream from the wiggler. Figure 3(b) shows the current density distribution $J_z(0,y)$ as a function of displacement in the y direction. This measurement is carried out by holding the antenna position fixed at $x = 0, y = 0$ and moving the entire waveguide in the y direction relative to the stationary electron beam. This determination is of course less accurate because of the considerable loss of symmetry caused by the waveguide displacement relative to the beam. The above measurements of the beam size and beam center are needed in understanding the subsequent RF intensity profiles.

To use the space-charge probe $I_x(SC)$ for the measurement of the RF fields, the DC beam current is shunted to ground, the RF field is rectified by a crystal diode and then displayed on a fast oscilloscope. Figure 4(a) illustrates how the electric field intensity $I_x(x,0)$ of the space charge wave varies as a function of the probe displacement in the x direction. We see that $I_x(x,0)$ is zero at the center of the electron beam, is maximum near the beam edge $x = r_b$ and falls off rapidly when $|x| > r_b$, in agreement with the expected behavior of the irrotational fields produced by the bunched electron beam. Figure 4(b) shows the variation in $I_x(0,y)$ as the antenna traverses the beam center in the y direction; and $I_x(r_b,y)$ gives the intensity variation as it traverses the beam edge. The small cartoons in the upper right hand corner illustrate schematically the motions of the space charge

probe. We note that these fields exist only during FEL activity, and become immeasurably small when, for example, the wiggler field is turned off or when the resonance conditions (1) and (2) are not fulfilled.

Combining data like that illustrated in Figure 4, one can generate a two-dimensional plot of the space charge field intensity profile. This is shown in Figure 5.

Since the space charge electric field points radially outwards from the electron beam center, it must undergo a 180° phase change in traversing the center. This effect is illustrated in Figure 6. Figure 6(a) shows a plot of the phase of the space charge wave as a function of time during the falling voltage pulse for two discrete positions of the antenna on opposite sides of the centre $x = \pm 4$ mm. Figure 6(b) gives the phase as a function of the antenna displacement in the x direction at a time during the pulse when the phase change is maximum (and the gain is near zero). It shows clearly the abrupt phase change when the beam center is crossed. This correct phase behavior also lends strong support to the validity of the observations of Figs. 2, 4 and 5, when the antennas are used in intensity measurements.

4. ELECTROMAGNETIC WAVE PROFILES

In this section we describe intensity and phase measurements using the movable antenna $I_y(EM)$ of Fig. 1. This antenna is oriented orthogonally to the space charge antenna $I_x(SC)$ of section 3, and is sensitive to electric fields E_y parallel to the direction y of the launched TE_{10} electromagnetic wave. In the absence of FEL activity measurements show that $I_y(EM)$ varies as $cos^2(\pi x/a)$ in accordance with expectations. This has been found to be so both in the absence of the electron beam (cold tests), and also in its presence, provided that the relevant FEL parameters were far removed from the resonance conditions (1) and (2).

In the presence of FEL activity the electric field intensity profile measured with antenna $I_y(EM)$ can be modified by one of two effects: optical guiding and contribution from the ambient space charge field $E_y(SC)$ of the bunched beam. Figure 7 illustrates the extent to which the RF profile is altered. In plotting the percentage change as a function of displacement, we subtract the underlying $cos^2(\pi x/a)$ variation.

The very substantial changes shown in Fig. 7 are in agreement with earlier measurements [14]. There, the observations were attributed to optical guiding. However, in view of the now available space charge field measurements of section 3 and recent theoretical input [12], [15] the earlier interpretation needs closer scrutiny. The point is, that the $I_y(EM)$ probe measures a signal that is proportional to $|E_y(EM)cos(\omega t - k_{\|}z) + E_y(SC)cos(\omega t - (k_{\|} + k_w)z)|^2$ which, after time averaging, consists of a sum of intensities $E_y^2(EM) + E_y^2(SC)$, and an interference term $2E_y(EM)E_y(SC)cos(k_w z)$. And, even if $E_y^2(SC) \ll E_y^2(EM)$, the interference term can produce significant profile modifications.

To be sure, the space charge electric fields are zero at the electron beam center and are large only near the beam edge $x = \pm r_b, y = \pm r_b$ (see Figs. 1, 4 and 5). Also, $E_y(SC)$ is by symmetry exactly zero along the x axis. Along the x axis, $E_y(SC)$ should not contribute to the overall intensity, were it not for the fact that the antenna has a finite length in the y direction($\sim$ 1 mm) and it can therefore pick up a small amount of y component of the space charge electric field. As a result, some contribution from $E_y(SC)$ occurs even along the x axis.

We have also carried out a series of measurements with the purpose of determining the relative amplitudes of the space charge and electromagnetic fields. We find that at spatial positions where each are at their maximum, the ratio $E_{SC}(r = r_b)/E_{EM}(r = 0) \approx 0.2$. This yields a value for the interference term whose magnitude is not inconsistent with the profile modifications shown in Fig. 7. To confirm this, we displaced the antennas axially by exactly half a wiggler period [such that $z' = z + l_w/2$] and performed a profile scan. The result is illustrated in Fig. 8. Comparing Figs. 7 and 8 we see that the profile "flipped over", an effect which must be attributed to a sign change in the interference term $2E_y(EM)E_y(SC)cos(k_w z)$. A scan of the phase shown in Fig. 9 exhibits a similar effect.

5. DISCUSSION

This paper is an experimental study of the quasi-electrostatic and electromagnetic fields, and their relative importance, generated during FEL activity. The experiments were performed in a Raman free electron laser under conditions where the collective effects due to the RF space charge cannot be neglected.

Section 3 is devoted to the study of the RF intensity and phase of the space charge fields. The spatial distribution of the transverse field component $E_x(SC)$ represents essentially the fringe fields of the space charge bunches generated during FEL activity. These fields vanish on the z axis and are antisymmetric, as is clearly demonstrated by Figs. 4, 5 and 6.

In section 4 we examine the transverse spatial profiles of the electromagnetic wave. The observed modification (Fig. 7), though originally believed to be due to optical guiding [14], is now ascribed to the presence of a small but not insignificant contribution from the space charge fields of the bunches. The space charge wave travels at a somewhat slower speed than the electromagnetic wave and the two waves are phase-locked to one another. This gives rise to wave interference, and to profiles like those shown in Fig. 7. A dramatic example of this interference effect is illustrated by comparing these profiles with those of Fig. 8, which were measured at a second axial position Z' displaced one half a wiggler period downstream. Phase measurements of Fig. 9 provide additional confirmation of the interference phenomenon. Any true optical guiding of the electromagnetic wave that may be present is masked by interference effects with the space charge wave.

Interference among the several [15] waves generated in an FEL interaction is also believed to be the cause of the following interesting effect that we have observed in the course of our measurements. Oscilloscope traces like those illustrated in Fig. 2(b) exhibit an overall temporal shift as a function of the transverse position x of the antenna used on making the measurement. This is shown in Fig. 10(a) in which the $I_y(EM)$ probe, positioned at different transverse positions, is used in the measurement of the RF output. We see that as $|x|$ increases, the gain peak as well as the absorption dip move to later times, that is, to lower electron beam energies γ. We ascribe this to wave interference among the several interacting waves [15] each characterized by slightly different detuning parameters $\delta(x) = \omega/v_{||} - k_{||}(x) - k_w$ and different transverse wave profiles. When the gain is low ($\sim$ 3 dB), as it is in our experiments, all interacting waves carry roughly the same weight. The observed temporal changes can be translated into corresponding changes in the beam energy parameter γ. This is illustrated in Fig. 10(b), where we plot the beam energy for maximum FEL gain, $\gamma_{max}(x)$, as a function of the transverse antenna position

x.

In conclusion, then, the experimental observations presented in this paper can serve as a basis for a detailed theoretical study of profile modifications in a Ramam FEL. To date, the theoretical analyses are in qualitative agreement with our measurements. However, there are large numerical differences. For example, theory predicts [12] that the ratio of the space charge to the electromagnetic field amplitude is ~ 0.02 which is about an order of magnitude smaller than the measured ratio. Similarly, the predicted change [15] in the temporal pattern as a function of transverse position x is much smaller than that obtained from the measurements like those shown in Fig. 10.

AKNOWLEDGEMENTS

This work was supported in part by the Air Force Office of Scientific Research and in part by the National Science Fundation.

REFERENCES

[1] P. Sprangle, R. A. Smith, and V. L. Granatstein, Infrared and Millimeter Waves, edited by K. J. Button (Academic, New York, 1979), Vol. 1, p. 279, and references therein. also N. M. Kroll, and W. A. McMullin, Phys. Rev. A**17**, 300 (1978).

[2] J. Fajans and G. Bekefi, Phys. Fluids **29**, 3461 (1986).

[3] J. Fajans, J. S. Wurtele, G. Bekefi, D. S. Knowles, and K. Xu, Phys. Rev. Lett. **57**, 579 (1986).

[4] T. J. Orzechowski, E. T. Scharlemann, and B. D. Hopkins, Phys. Rev. A **35**, 2184 (1987).

[5] P. Sprangle and C. M. Tang, Appl. Phys. Lett. **39**, 677 (1981).

[6] W. M. Kroll, P. L. Morton, and M. W. Rosenbluth, IEEE J. Quantum Electron. **17**, 1436 (1981).

[7] J. M. Slater and D. D. Lowenthal, J. Appl. Phys. **52**, 44 (1981).

[8] D. Prosnitz, A. Szoke, and V. K. Neil, Phys. Rev. A **24**, 1436 (1981); also D. Prosnitz, R. A. Haas, S. Doss, and R. J. Gelinas, in *Free Elecctron Generators of Coherent Radiation*, Physics of Quantum Electronics Vol. 9, edited by Stephen F. Jacobs, Murray Sargent, III, and Marlan O. Scully (Addison-Wesley, Reading, MA, 1982), p. 1047.

[9] E. T. Scharlemann, A. M. Sessler, and J. S. Wurtele, Phys. Rev. Lett. **54**, 1925 (1985).

[10] G. T. Moore, Opt. Commun. **52**, 46 (1984), and Nucl. Instrum. Methods Phys. Res. Sect. A **239**, 19 (1985).

[11] J. Fajans, J. Appl. Phys. **55**, 43 (1984).

[12] E. Jerby and A. Gover (to be published in Phys. Rev. Letters).

[13] H. P. Freund and P. Sprangle, Phys. Rev. A **28**, 1835 (1983).

[14] F. Hartemann, K. Xu, G. Bekefi, J. S. Wurtele and J. Fajans, Phys. Rev. Lett. **59**, 1177 (1987).

[15] J. Fajans and J. S. Wurtele (to be published in Phys. Fluids).

FIGURE CAPTIONS

Figure 1 Schematic diagram of the experimental arrangement showing the placement of the probing antennas.

Figure 2 Oscilloscope traces of (a) the beam voltage; (b) RF field intensity of the electromagnetic wave; (c) intensity of the space charge wave; and (d) RF phase of the electromagnetic wave (see text). The straight lines in (b), (c) and (d) are traces when the beam is kicked out of the system 18 cm upstream from the antennas, thereby terminating FEL activity at that point. The experimental parameters are: $B_{||} = 1580$ G; $Bw = 130$ G; $\omega/2\pi = 9.7$ GHz; $I \simeq 1$ A; RF power input= 3 W.

Figure 3 DC current density profile $J_z(x, y)$ of the electron beam, measured at the position of the dipole antennas.

Figure 4 Transverse field intensity profiles of the space charge (ponderomotive) wave of the bunched electron beam at a time of maximum FEL gain. The cartoons in the upper right hand corner illustrate the directions of scan. The experimental parameters are the same as in the caption to Fig. 1 except that $B_w = 200$ G, $I \simeq 4$ A.

Figure 5 Two dimensional presentation of the transverse field intensity profile of the space charge wave at a time of maximum FEL gain. The experimental parameters are the same as in Fig. 4.

Figure 6 Transverse phase profile of the space charge wave at a time of maximum phase change (a) as a function of time during the voltage pulse; (b) as a function of antenna position at a time near zero gain (see text). The experimental parameters are the same as in Fig. 4.

Figure 7 Two dimensional distribution of $I_y(EM)$ (the normalized electromagnetic wave intensity) at an axial position $z \simeq 115$ cm and at a time of maximum gain. The experimental parameters are the same as in Fig. 2.

Figure 8 Two dimensional distribution of $I_y(EM)$ (the normalized electromagnetic wave intensity) at an axial position $z' = z + l_w/2$ and at a time of maximum gain. The experimental parameters are the same as in Fig. 2.

Figure 9 Phase distribution as a function of transverse displacement at a time of maximum

phase change (near zero gain) at (a) $z = 115$ cm and (b) $z' = z + l_w/2$. The experimental parameters are the same as in Fig. 2.

Figure 10 (a) Oscilloscope traces (cf Fig. 2) of the beam voltage and of the intensity $I_y(EM)$ for 4 different positions x of the probing antenna, showing overall pattern shift to lower voltages. (b) beam energy parameter $\gamma_{max}(x)$ at maximum gain as a function of the axial displacement x.

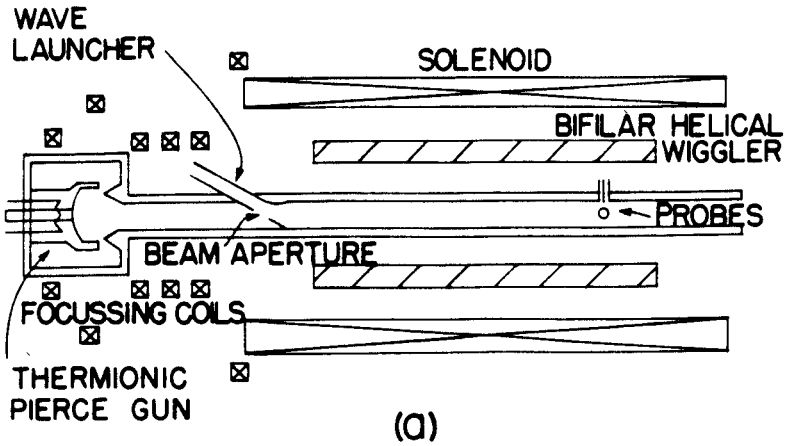

(a)

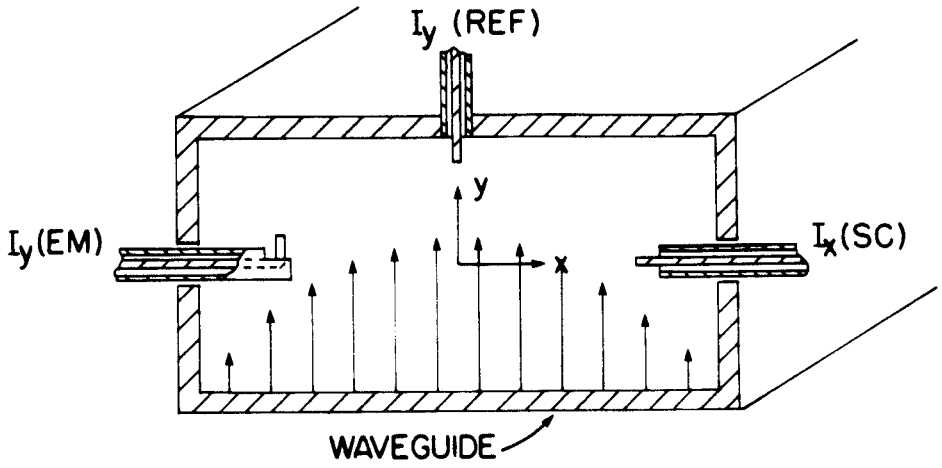

(b)

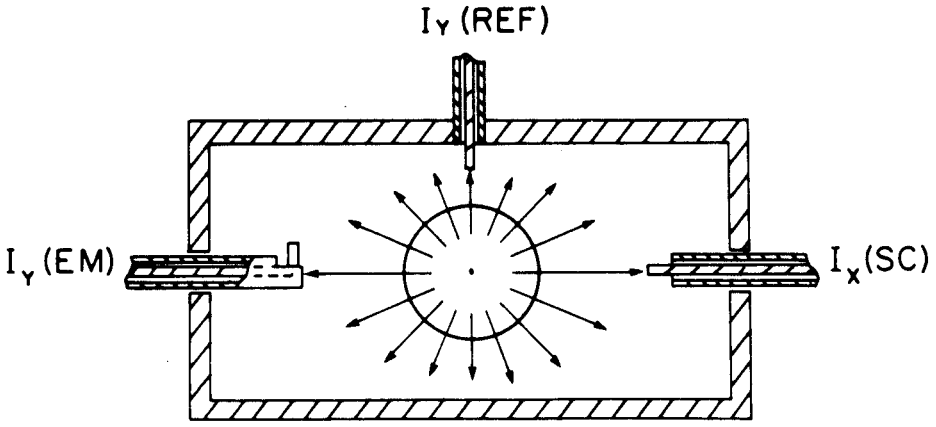

(c)

Fig.1 Xu,Bekefi,Leibovitch

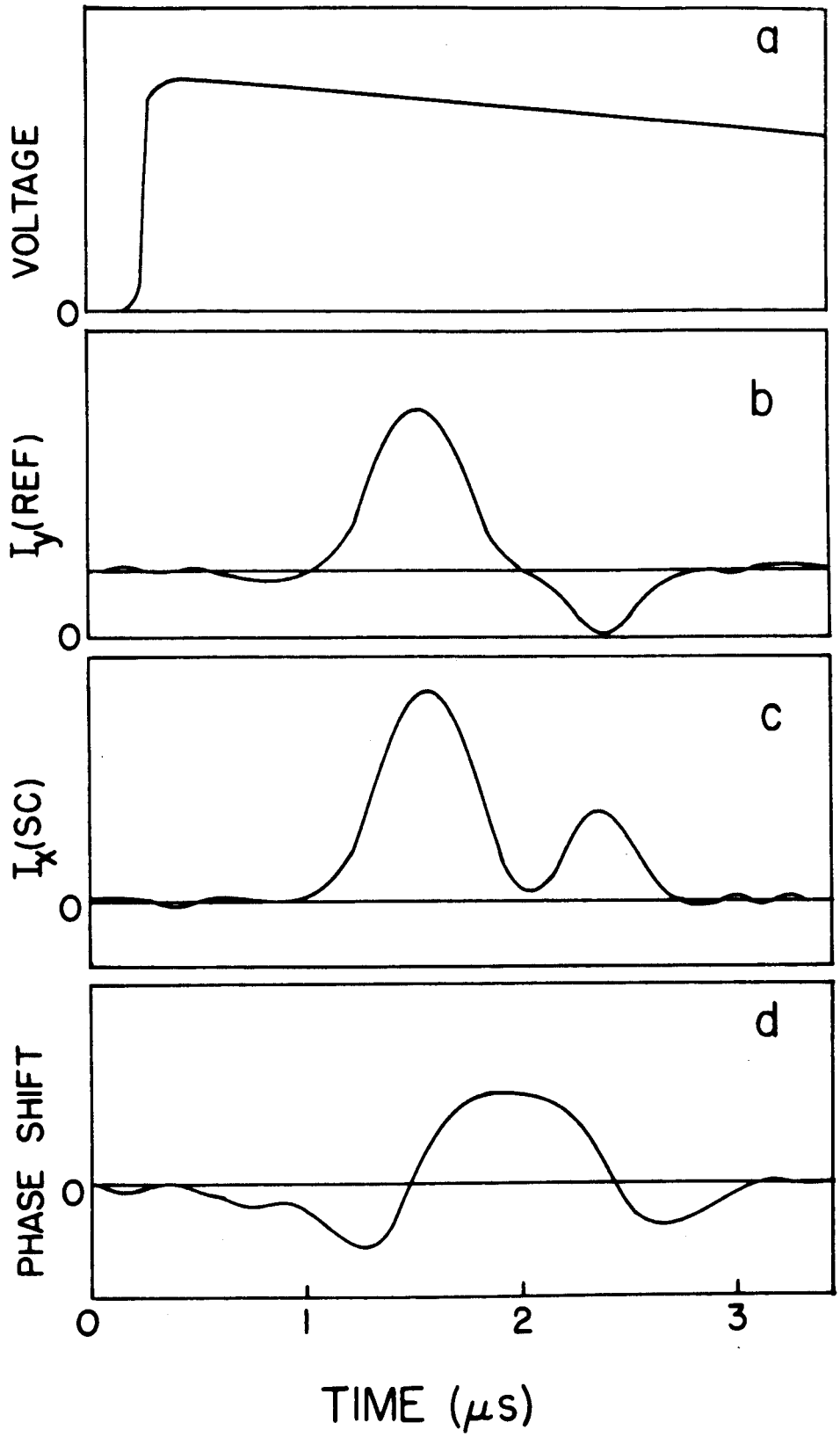

Fig.2 Xu,Bekefi,Leibovitch

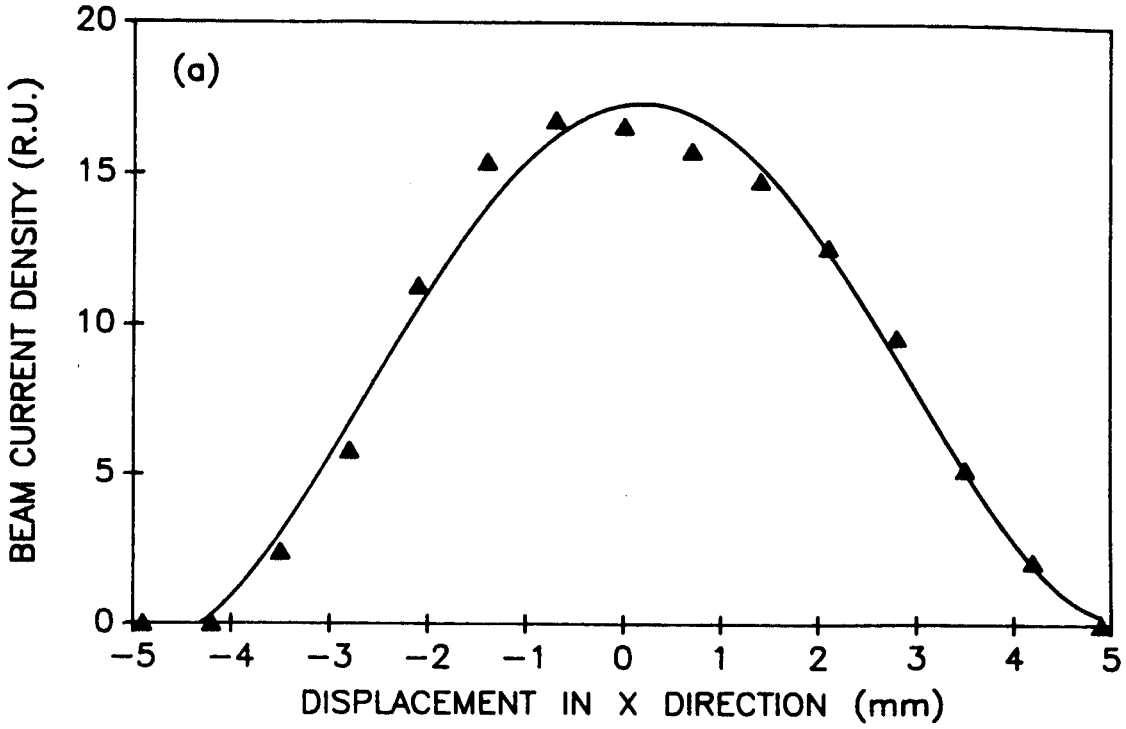

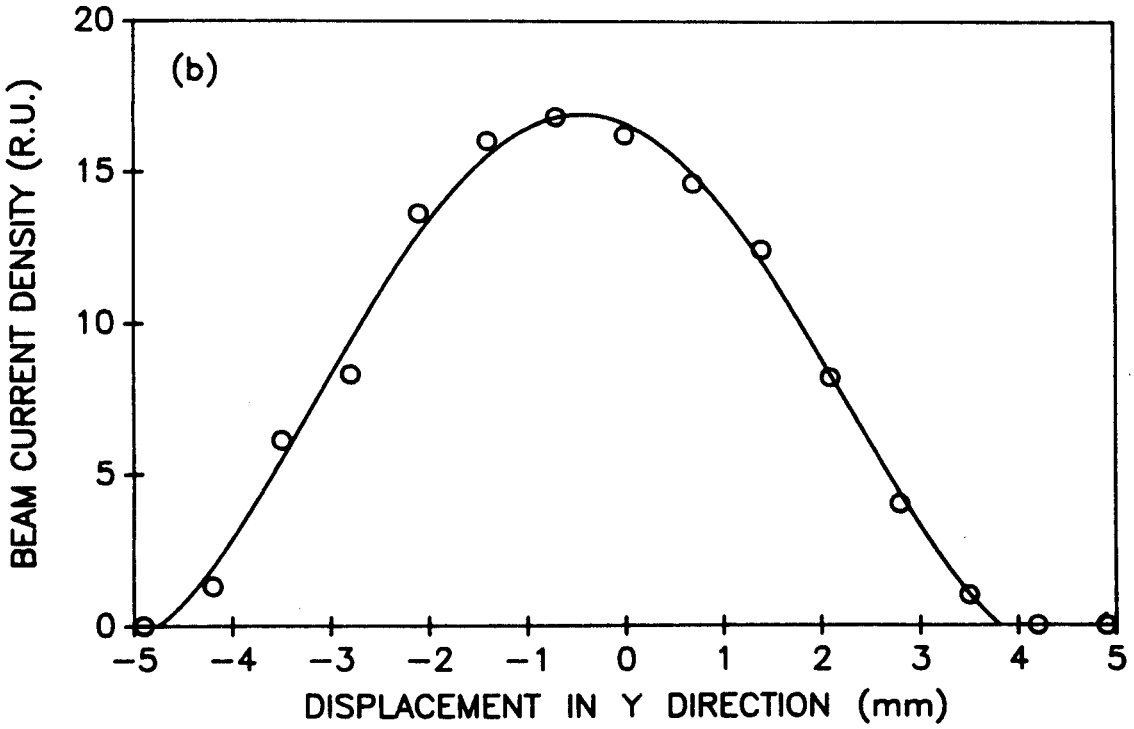

Fig.3 Xu,Bekefi,Leibovitch

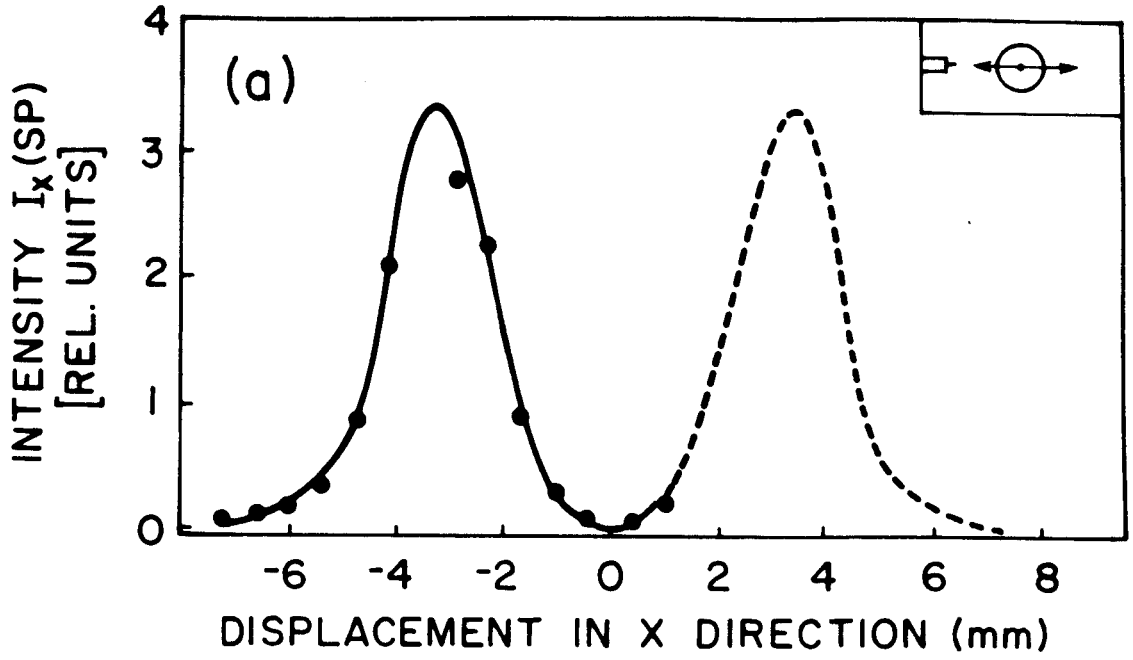

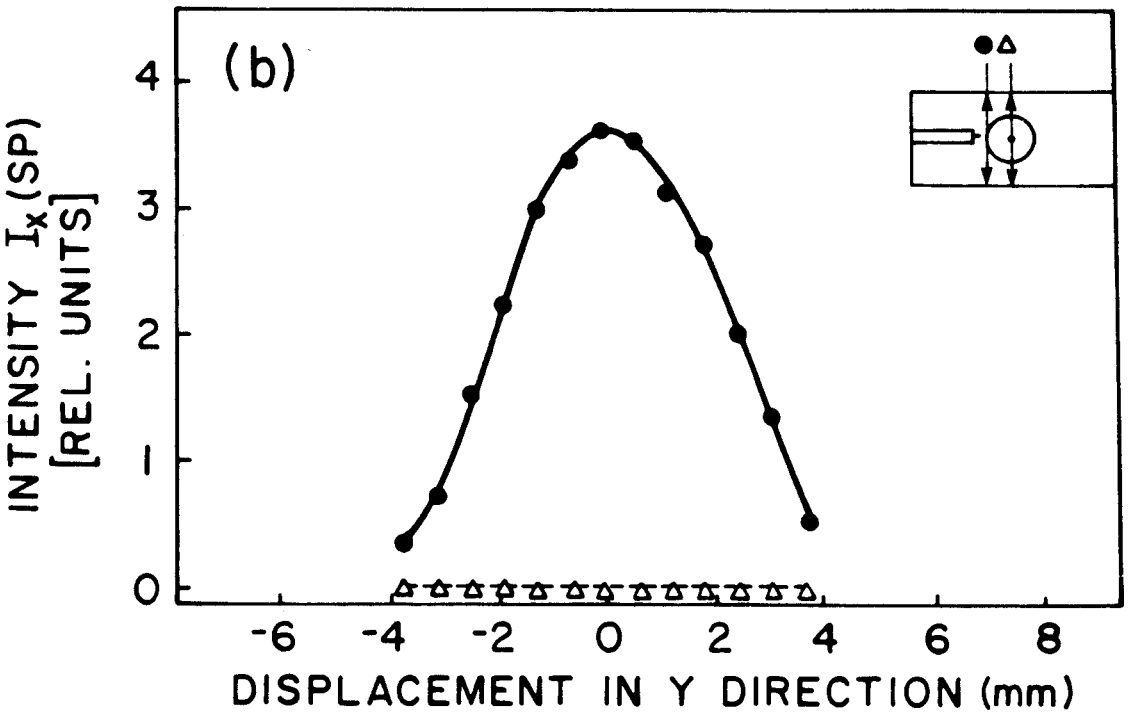

Fig.4 Xu,Bekefi,Leibovitch

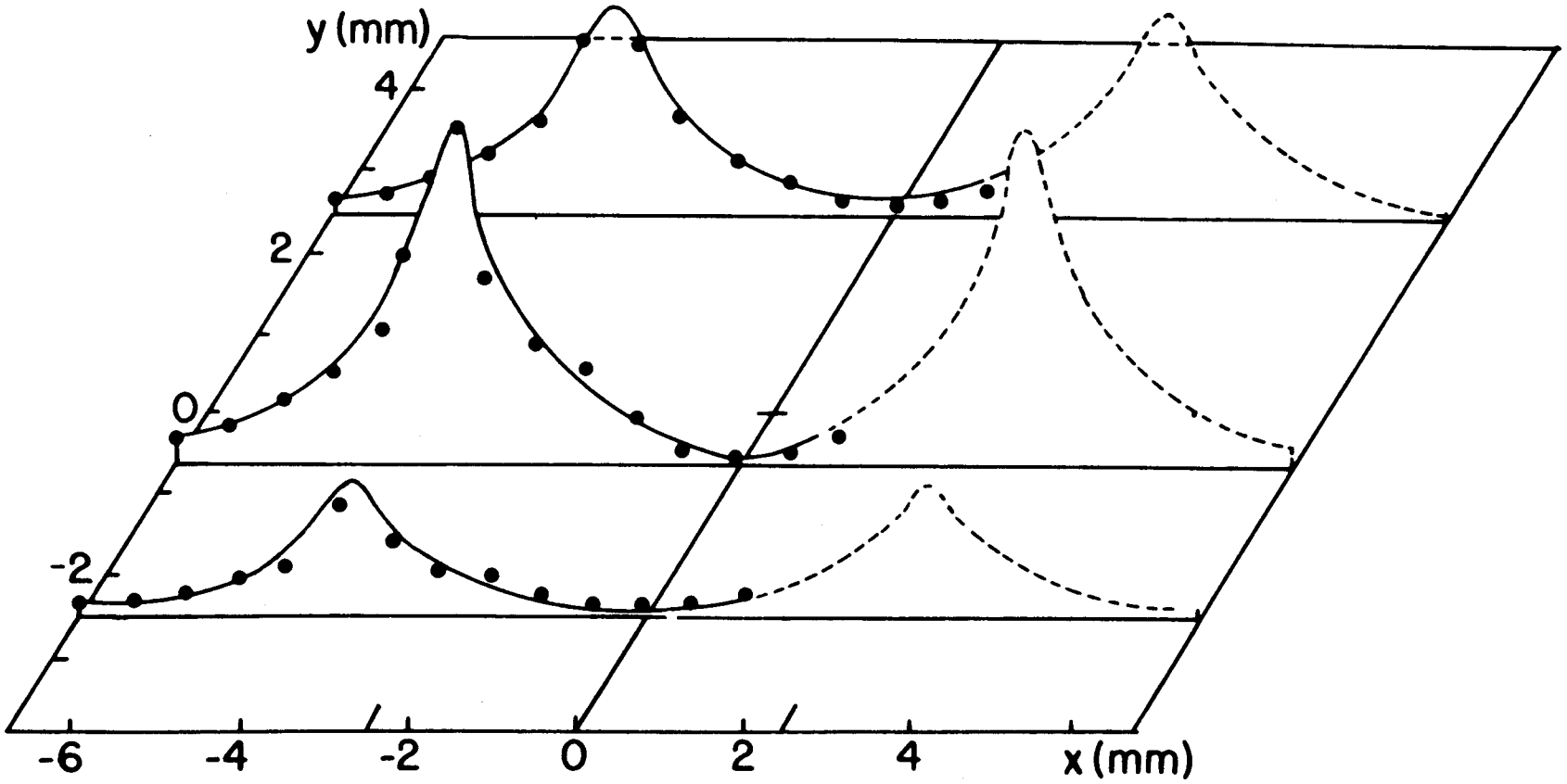

Fig.5 Xu,Bekefi,Leibovitch

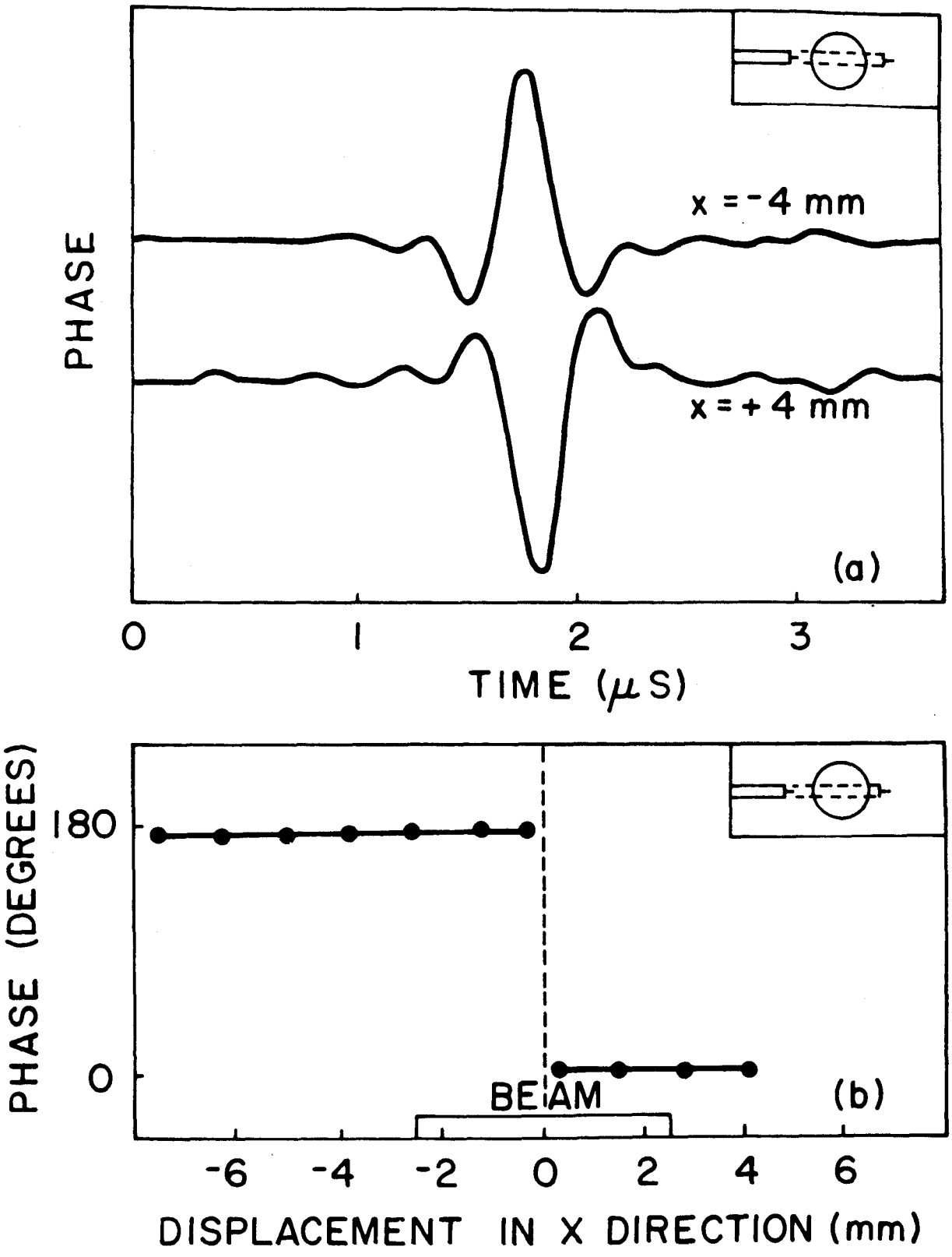

Fig.6 Xu,Bekefi,Leibovitch

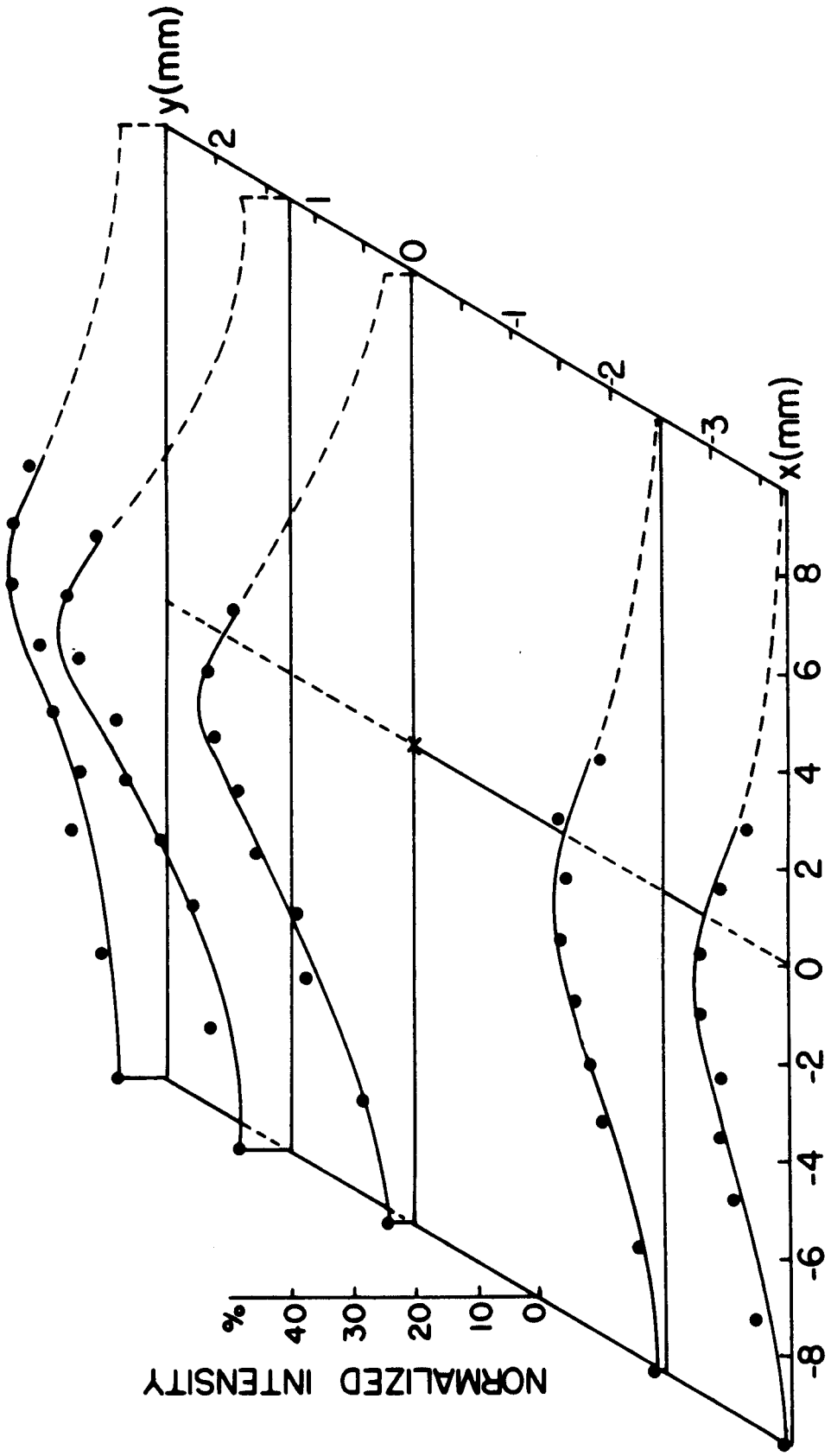

Fig.7 Xu,Bekefi,Leibovitch

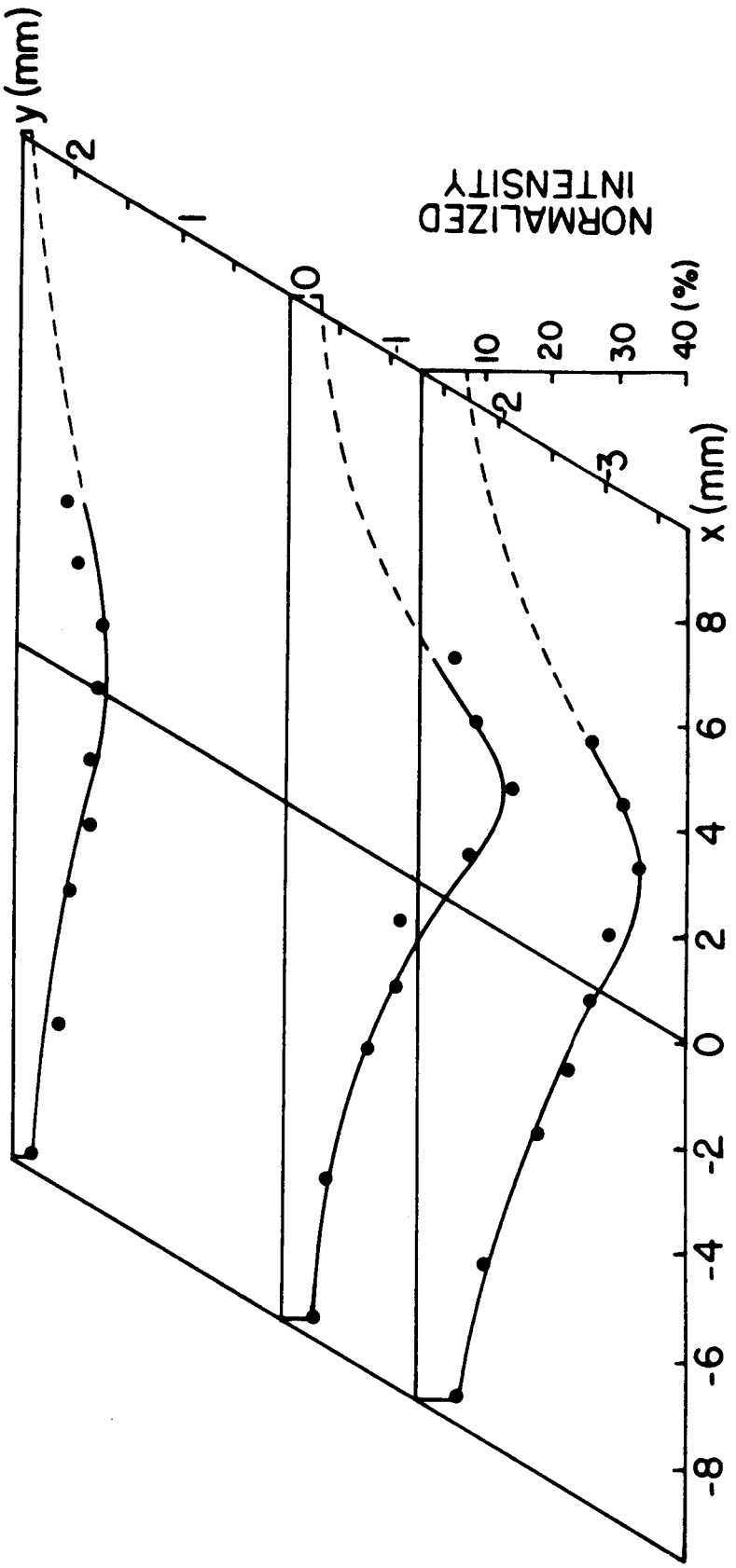

Fig.8 Xu,Bekefi,Leibovitch

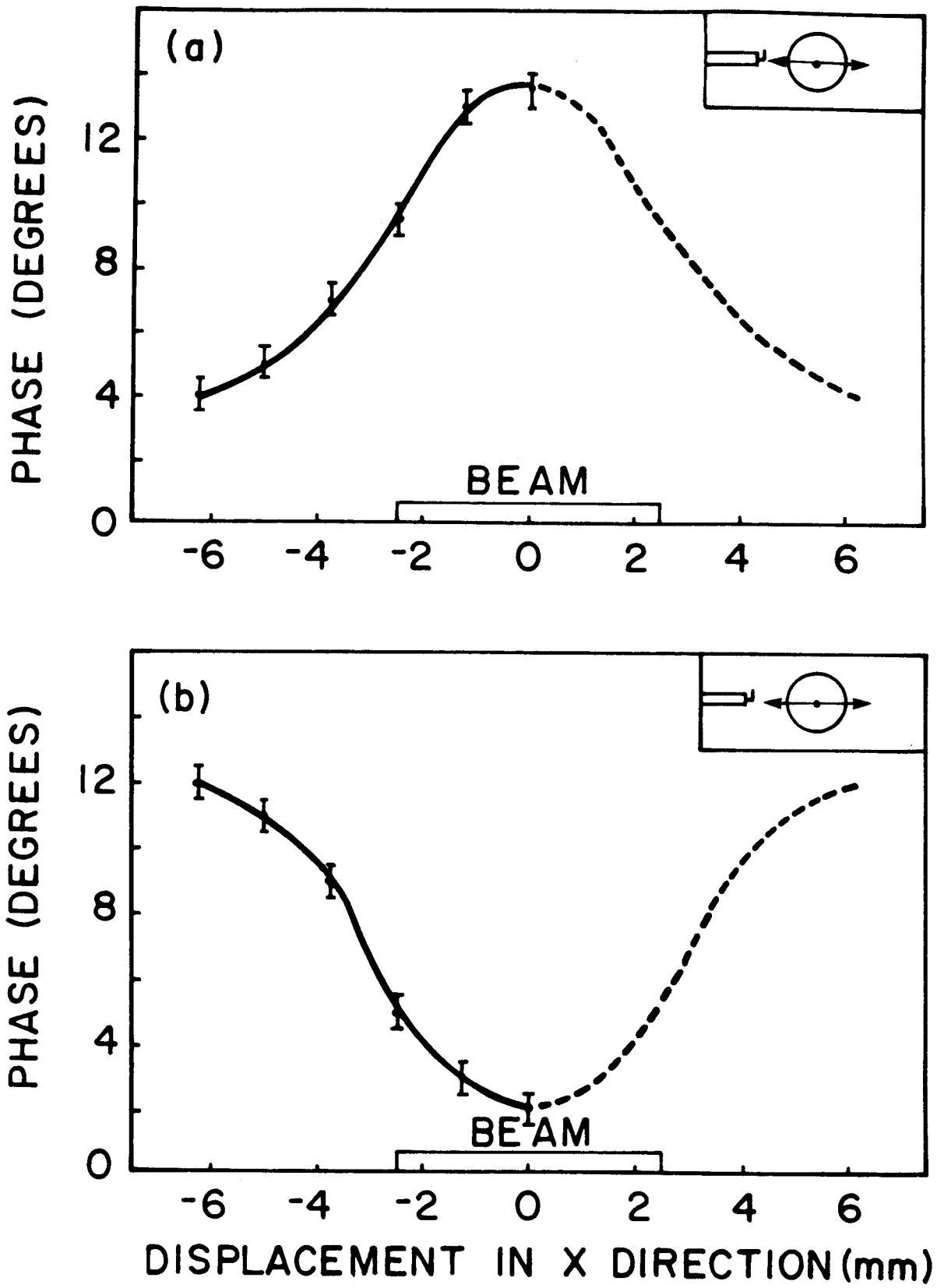

Fig.9 Xu,Bekefi,Leibovitch

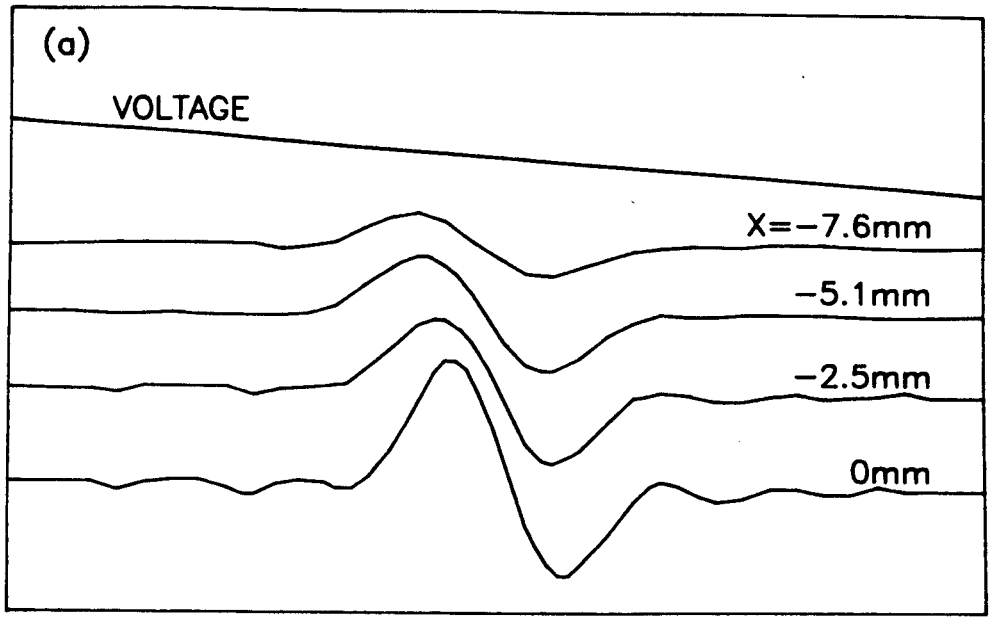

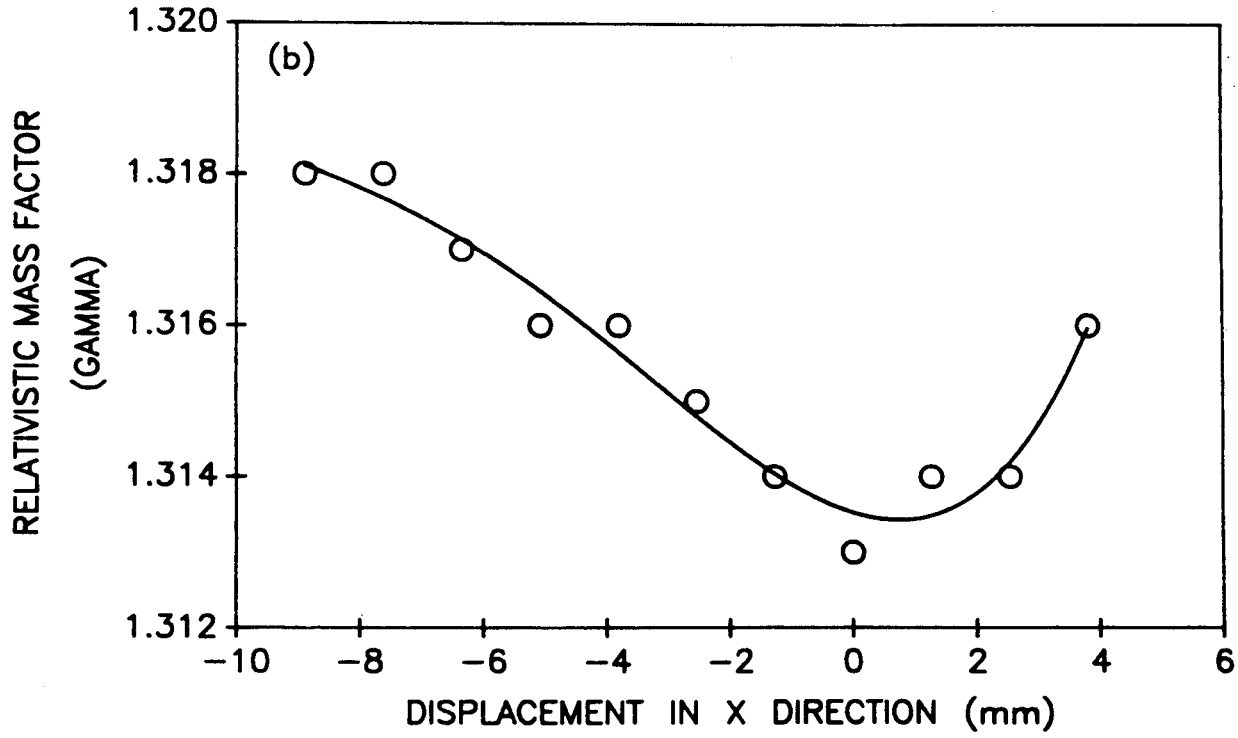

Fig.10 Xu,Bekefi,Leibovitch